Enhanced catalytic activity of nanostructured, A-site deficient $(La_{0.7}Sr_{0.3})_{0.95}(Co_{0.2}Fe_{0.8})O_{3-\delta}$ for SOFC cathodes

Ozden Celikbilek[a,b*], Cam-Anh Thieu[c,d], Fabio Agnese[e], Eleonora Cali[b], Christian Lenser[f], Norbert H. Menzler[f], Ji-Won Son[c,d], Stephen J. Skinner[b], Elisabeth Djurado[a]

a. Univ. Grenoble Alpes, Univ. Savoie Mont Blanc, CNRS, Grenoble INP, LEPMI, 38000, Grenoble, France
b. Department of Materials, Imperial College London, Prince Consort Road, London SW7 2BP, United Kingdom
c. Center for Energy Materials Research, Korea Institute of Science and Technology (KIST), Hawolgok-dong, Seongbuk-gu, Seoul 02792, Korea
d. Division of Nano & Information Technology, KIST School, Korea University of Science and Technology (UST), Hawolgok-dong, Seongbuk-gu, Seoul 02792, Korea
e. Univ. Grenoble Alpes, INAC-SyMMES, F-38054 Grenoble Cedex 9, France.
f. Forschungszentrum Jülich GmbH, Institute of Energy and Climate Research: Materials Synthesis and Processing (IEK-1), 52425 Jülich, Germany

*Corresponding author: o.celikbilek@imperial.ac.uk

Abstract

Lower operating temperatures (≤ 650 °C) of solid oxide fuel cells (SOFCs) are sought in order to decrease the system costs and improve material compatibility and durability issues. Here, we report A-site deficient $(La_{0.7}Sr_{0.3})_{0.95}(Co_{0.2}Fe_{0.8})O_{3-\delta}$ (LSCF) perovskite film as a potential high-performance cathode with microstructural details at the nanometre length scale. This cathode exhibits area specific resistance value of as low as 0.037 Ω cm^2 in a symmetrical cell and peak power density of 1.4 W cm^{-2} in a Ni/YSZ anode-supported cell at 650 °C. X-ray diffraction and electron microscopy analyses revealed a closely related two-phase perovskite structure for LSCF and a well-dispersed, nanoscale B-site spinel phase ($CoFeO_x$) decorating the LSCF surfaces. Detailed investigations were carried out to correlate the surface to bulk elemental composition changes on the film, the catalytic activity of the spinel phase and the crystal structures of the constituents with the oxygen reduction reaction (ORR) kinetics. The oxygen transport parameters calculated from the electrochemical impedance spectra indicate an increase by one-to-two-orders of magnitude in the oxygen surface-exchange coefficient (k_o) in comparison to nominally stoichiometric, benchmark material $La_{0.6}Sr_{0.4}Co_{0.2}Fe_{0.8}O_{3-\delta}$. Such substantial improvements in the electrode performance were attributed to the catalytically active B-site spinel phase created by the A-site deficiency and to the very high active surface area of the film.

1. Introduction

Lower operating temperatures in solid oxide fuel cells (SOFC) opens up new opportunities for mobile/transport applications, where quick start-up time is of great importance.[1] However, the low-temperature operation requires high-performance electrodes to overcome sluggish reaction kinetics in existing materials. Typically, two approaches are considered to improve the electrode performance at low temperatures; the first is based on the microstructural design considering morphological requirements, and the second is on the material choice.

Particle/pore size control, electrode thickness and current collection, connectivity between particles, facile gas diffusion and adhesion to the electrolyte are the areas of focus for microstructural design[2]. All these parameters are influenced by the processing, which consists of material synthesis, coating technique and thermal treatments. On the other hand, oxygen surface exchange and diffusion parameters, ionic and electronic conductivity as well as the stability during operation and stability with the other components of the cell are considered for material selection.[3] Composites[4], surface decoration with nano-sized particles[5] or *in situ* forming of secondary phases[6] are implemented to improve cathodes.

Moreover, slight A- or B-site excess/deficiency in the ABO_3-type family of perovskites is shown to influence all the parameters above.[7] Notably, A-site deficiency was intentionally introduced to create additional oxygen vacancies to improve the ionic conductivity and the stability of a phase.[8] However, a very narrow stability regime was shown for these materials.[9] Deviation from A:B, as small as $0.997 < A:B < 1.003$, results in the formation of a Ruddlesden-Popper type layered perovskite in the case of A-site excess and a spinel oxide in the case of B-site excess.

Contradictory results were presented for the influence of the A-site non-stoichiometry and consequent secondary phase formations on the electrochemical properties of ABO_3 perovskites. While one study showed lower resistance in a highly A-site deficient case[10], another one showed that precipitates formed after excess A-site or B-site cation additions neither improved nor deteriorated the cell performance.[11] A recent study showed beneficial effects in an A-site deficient case for reducing chromium poisoning degradation by forming Cr- doped B-site spinels at the nanometre length scale.[12] On the contrary, another work studying A-site deficient ABO_3 revealed insulating secondary phase formations at the cathode/electrolyte interface, which mitigated the other beneficial effects that were created with A-site deficiency.[13]

Among well-studied ABO_3 type perovskites, $(LaSr)(CoFe)O_{3-\delta}$ (LSCF) showed continuous operation for years with negligible degradation.[14,15] There is still a great deal of interest to seek new compositions of non-stoichiometric LSCF at the A- or B-site. It is, however, unclear how the catalytic activity is affected by secondary phase formations resulting from changes in the stoichiometry.

In this work, we evaluate $(La_{0.7}Sr_{0.3})_{0.95}(Co_{0.2}Fe_{0.8})O_{3-\delta}$ (5 % A-site deficient LSCF 7328) films by structural, microstructural, and electrochemical characterisation techniques. The films deposited by the electrostatic spray deposition (ESD) technique have so far shown one of the lowest area specific resistance (ASR) values in the literature, recording 0.021 and 0.065 Ω cm^2 at 650 and 600 °C, respectively at OCV.[16] Microstructural features at the nanometre length scale are amongst the key factors for improved electrode performance. However, the enhanced catalytic behaviour of our LSCF cathode cannot be solely explained by the microstructure. Scanning electron microscopy (SEM), powder X-ray diffraction (XRD), high-resolution transmission electron microscopy (HR-TEM), scanning transmission electron microscopy (STEM) coupled with energy dispersive X-ray spectroscopy (EDX), low energy ion scattering spectroscopy (LEIS) and electrochemical impedance spectroscopy (EIS) were employed to study the cathode thoroughly and to explain such large improvements in its performance.

2. Experimental Section

The symmetric cells (electrode / $Ce_{0.9}Gd_{0.1}O_{2-\delta}$ (GDC) / electrode) were prepared from a double layer architectured electrode consisting of a functional layer (FL) of LSCF deposited by the ESD and topped by a screen-printed (SP) current collecting layer (CCL) of the same material. The GDC pellets (19.6 mm in diameter, 1 mm thick) were fabricated by uniaxial and isostatic (300 MPa) pressing of GDC powder (Praxair, 99.9%, 20.5 m^2 g^{-1}). These pellets are then sintered at 1200 °C for 2 h in air and then polished to obtain a flat and uniform surface.

The targeted stoichiometry of the LSCF was $La_{0.6}Sr_{0.4}Co_{0.2}Fe_{0.8}O_{3-\delta}$ (LSCF 6428). However, analysis by inductively coupled plasma-optical emission spectrometry (ICP-OES) (iCAP 6500 Thermo Scientific, USA) showed the average stoichiometry of the film to be $(La_{0.71}Sr_{0.29})_{0.95}Co_{0.17}Fe_{0.83}O_{3-\delta}$. It was simplified to $(La_{0.7}Sr_{0.3})_{0.95}Co_{0.2}Fe_{0.8}O_{3-\delta}$ in the text and will be referred to as 5% A-site deficient LSCF 7328.

Films were deposited using a vertical ESD setup starting from precursor salt solutions. Appropriate amounts of $La(NO_3)_3.6H_2O$ (Prolabo, 99.99%), $SrCl_2.6H_2O$ (Strem Chemicals, 99%), $Co(NO_3)_2.6H_2O$ (Sigma-Aldrich, 99.999%) and $Fe(NO_3)_2.9H_2O$ (Sigma-Aldrich, 99.99%) salts were dissolved in absolute ethanol (C_2H_5OH, 99.9%; Prolabo) and butyl carbitol ($CH_3(CH_2)_3OCH_2CH_2OCH_2CH_2OH$, 99+%; Acros Organics) with a 1:2 volume ratio and a total salt concentration of 0.02 mol L^{-1}. The solution was sprayed onto the substrate. The homogeneity of the deposition was ensured by moving the substrate in x and y directions at a controlled speed of 1 mm s^{-1}. ESD deposition parameters comprise a substrate temperature of 300 °C, a nozzle to substrate distance of 15 mm, the voltage of ~5-6 kV, and flow rate of 1.5 mL h^{-1} for 1h 45 min of deposition. Films were sintered at 900 °C for 2 h at a 2 °C min^{-1} heating rate and a 3 °C min^{-1} cooling rate.

A commercial LSCF ink ($La_{0.62}Sr_{0.38}Co_{0.19}Fe_{0.8}O_{3-\delta}$ powder from Marion Tech. $d_{50} = 0.27$ μm) was screen-printed symmetrically onto the ESD films as CCLs for electrochemical impedance spectroscopy measurements.[17]

The morphology of the ESD films was investigated by SEM with a field emission gun (ZEISS Ultra 55) operating at an accelerating voltage of 3 kV and an average of 7 mm working distance. The samples were coated with Pt to avoid electrons charging.

XRD was performed using a Panalytical XPERT-PRO-diffractometer. The data were collected in the Bragg–Brentano geometry in the 2θ range from 20 to 100° with a 0.017° step size and a 1-second step time. The phase identification was carried out using the International Centre for Diffraction Data database (ICDD). The cell parameters were obtained by refinement using the Fullprof software suite.[18]

The LSCF particles were removed from the surface of GDC electrolyte with a spatula for HR-TEM observations. The analysis on the structure and elemental composition were carried out on a JEOL 2100F microscope equipped with an Oxford Instruments EDX detector. EDX was performed in STEM mode with annular dark field detector.

To isolate the catalytic effect of the B-site precipitates ($CoFeO_x$, simply CFO) and to mimic the small particle size of the CFO similar to the ESD films, new experiments based on infiltration were designed with the nominally stoichiometric $La_{0.6}Sr_{0.4}Co_{0.2}Fe_{0.8}O_{3-\delta}$ cathodes (Sigma-Aldrich, 10-14 m^2/g). An ink of stoichiometric LSCF 6428 powder was screen-printed onto GDC substrates and the films were subsequently sintered at 950 °C for 2h in air. 0.6 M, 6 µL CFO solution (1:1 ethanol: deionised water) was infiltrated into the LSCF backbone to obtain particles at the nanometre length scale. The loading of the CFO was estimated to be ~4 wt. % after the burning out of the solvent and the nitrates. The sample was first heated at 350 °C for 30 min to dry up, and then its impedance was taken at each 50 °C increase from 450 to 750 °C and then similarly on cooling.

Qtac100 (IonTOF Gmbh, Germany) low energy ion scattering (LEIS) spectrometer was used to probe the outermost atomic layer of the surface.[19] The intensities of the backscattered ions are directly proportional to the amount of each chemical species covering the surface. $^{20}Ne^+$ was used as a primary ion to separate the cation peaks and determine the surface composition. LEIS depth profiles of a few nanometres were obtained with 1 keV $^{40}Ar^+$ sputter beam at a sputtering angle of 60 degrees. The sputtered area was 1×1 mm^2 whereas the analysis area of the primary beam was 0.75×0.75 mm^2. An oxygen plasma cleaning of the surface was done prior to the analysis. For the depth profile, the peak areas of each cation were normalised to the total sum of each peak area. Increasing Ar dose corresponds to the chemical composition below the surface. Surface Lab 6 software (IonTOF GmbH, Germany) with Gaussian peaks of different elemental components with the background was used to fit the peaks.

Impedance spectroscopy was used for electrochemical characterisations. Symmetrical cell measurements in open circuit voltage (OCV) mode were carried out in the static ambient air with 50 °C temperature steps from 450 to 650 °C using an Autolab frequency response analyser operating between 10 kHz and 0.05 Hz. The amplitude of the measuring signal was adjusted to 20 mV. The deposited films were contacted with Pt grids (Heraeus, 3600 meshes cm^{-2}) and then sandwiched between Al_2O_3 blocks with gas channels, which were pressed to ensure maximum contact points. Nyquist and Bode representations of the EIS data were fitted with electrical equivalent circuits using the EC-Lab® software (V10.44).

Single cell tests were performed on anode-supported cells prepared at Forschungszentrum Jülich, Germany. The cells were based on tape-cast NiO-YSZ supports of ~300 µm thickness, and screen-printed NiO-YSZ anodes were obtained from CeramTec GmbH (Marktredwitz, Germany). The 1.5 µm thin YSZ electrolyte was prepared by the sequential deposition of YSZ nano-dispersion and polymeric sol, followed by co-sintering of the half-cell at 1400 °C.[20] Subsequently, a ~ 0.5 µm thin $Gd_{0.2}Ce_{0.8}O_{1.9}$ diffusion barrier layer was deposited via Magnetron Sputtering. The LSCF cathode prepared via ESD had 10 x 10 mm^2 dimension. A-site deficient $La_{0.58}Sr_{0.4}Co_{0.2}Fe_{0.8}O_{3-\delta}$ ink (FZJülich, Germany) was screen printed on the LSCF films deposited by the ESD to serve as CCL and sintered at 850 °C for 2 h in air. Measurements were performed in the temperature range of 450-650 °C, using an Iviumstat test apparatus in a frequency range between 1 MHz and 0.1 Hz. Air on the cathode side and humidified H_2 on the anode side with a fuel composition of 97 vol. % H_2 and 3 vol. % H_2O at a flow rate of 200 standard cm^3 min^{-1} (sccm) was used. A modified interconnect rib design with gold mesh with openings of 250 µm by 250 µm were used for the cell test. Current vs voltage data were recorded between 650 °C and 450 °C at each 50 °C in descending order. A Solartron impedance analyser with an electrochemical interface (SI 1260 and SI 1287, Solartron) and an Iviumstat electrochemical analyser (Iviumstat, Ivium Technologies) was used to obtain these EIS and I-V-P curves. The AC amplitude of the impedance measurements was set to 50 mV.

3. Results and Discussion

The ESD technique helps to obtain nanometre length scale features, high crystallinity, and good adhesion to the electrolyte at low sintering temperatures (~ 800-900 °C for 2 h in air). In Fig. 1a, plan view micrographs show approximately 1-2 µm wide interconnected gas diffusion channels separating the large columnar-like blocks. The particle and porosity sizes within the columns are rather homogeneous and remain within 100 nm. Nano-scale porosity within the columnar blocks connects to the large gas diffusion channels and helps diffuse the oxygen gas (Fig. 1b). Cross-sectional views of LSCF films deposited on GDC electrolytes (Fig. 1c) and on an anode supported cell (Fig. 1d) show that the films were approximately 10 µm-thick and adhered well to the electrolyte. The porosity, specific surface area and tortuosity within the columnar blocks of LSCF films sintered at 800 °C for 2h were previously calculated from reconstructed FIB-SEM images.[16] The small-scale features gave specific surface area values of as high as 19 ± 6 μm^{-1}, porosity values within 22 ± 7 %, and tortuosity values of 1.50 ± 0.2. In this study, the film sintering temperature was set at 900 °C, as the sealing procedure for full fuel cell tests required heating the cells to 800 °C for 100 h. From the SEM images, higher sintering temperature appeared to increase the particle size slightly, but the porosity remained similar.

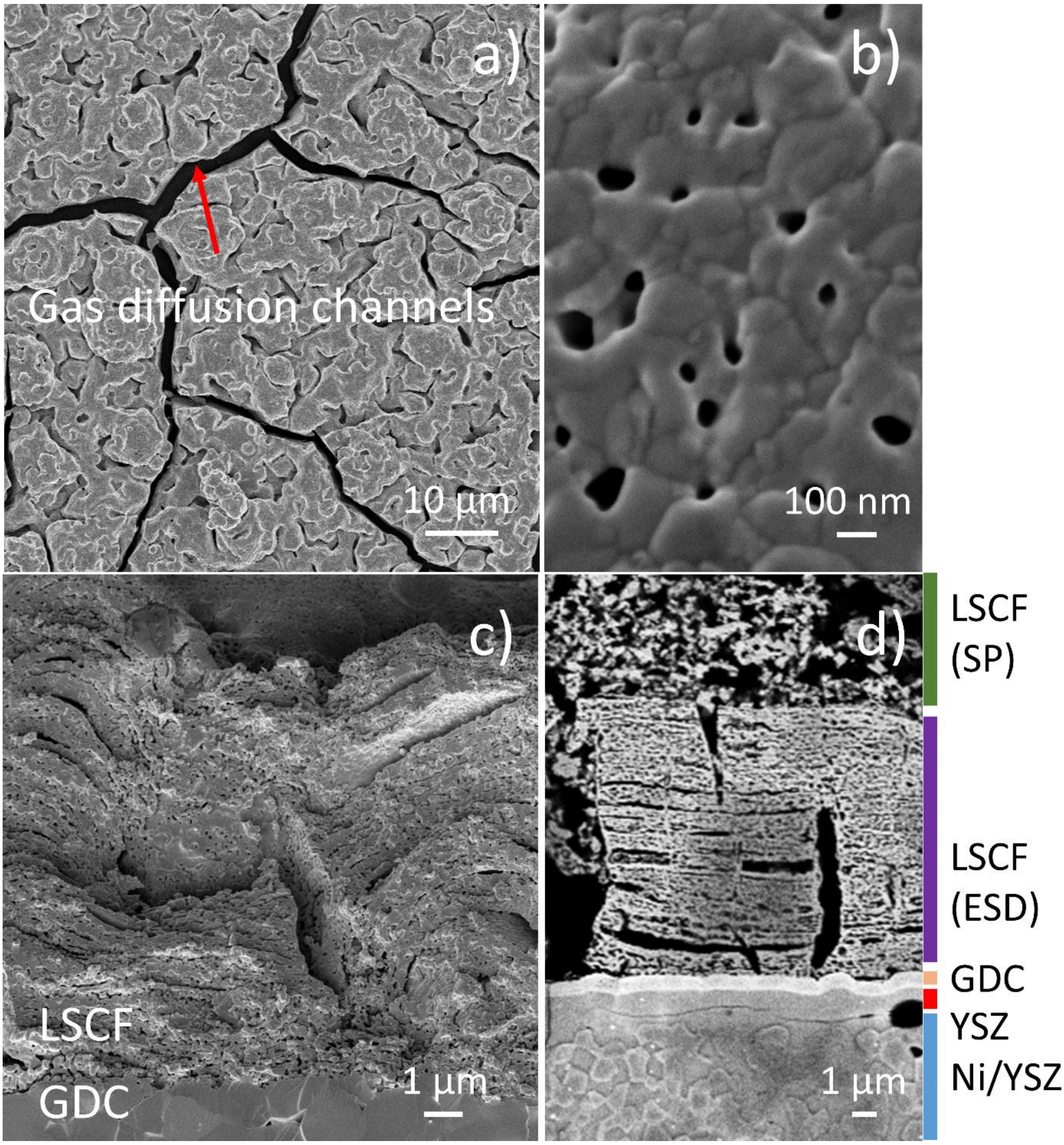

Fig. 1. a-b) Plan view SEM micrographs of LSCF film sintered at 900 °C for 2 h in air, Cross-sectional SEM micrograph of c) LSCF film on GDC electrolyte and d) As-deposited LSCF film on anode-supported bi-layer electrolyte cell. The coloured bars next to d) show each layer in the cell.

The XRD patterns and the structural refinement of the functional layer on GDC electrolyte support are shown in Fig. 2. The vertical lines under the diagram correspond well to the ICDD database for the LSCF 6428 phase (ICDD: 04-020-8368) with $R\bar{3}c$ space group (No. 167) and the GDC phase (ICDD: 04-012-3418) with $Fm\bar{3}m$ space group (No. 225). The diffraction pattern of the third phase corresponds well to a spinel crystal structure ($Fd\bar{3}m$) with a unit cell parameter equal to a = 8.3204(7) Å. The lattice parameter of the cubic GDC phase is refined to 5.4189(2) Å. The refinement of the LSCF with one rhombohedral phase did not yield a good fitting (Fig. 2, Table 1). Two rhombohedral phases with slightly different *a*, *b* and *c* parameters gave an improved fit. Similar behaviour was observed in previous reports on A-site non-stoichiometric LSCF.[10] The first phase was fitted with *a*, *b* = 5.48(8) Å and *c* = 13.50(2) Å and the second phase was fitted with *a*, *b* = 5.47(9) Å and *c* = 13.56(4) Å.

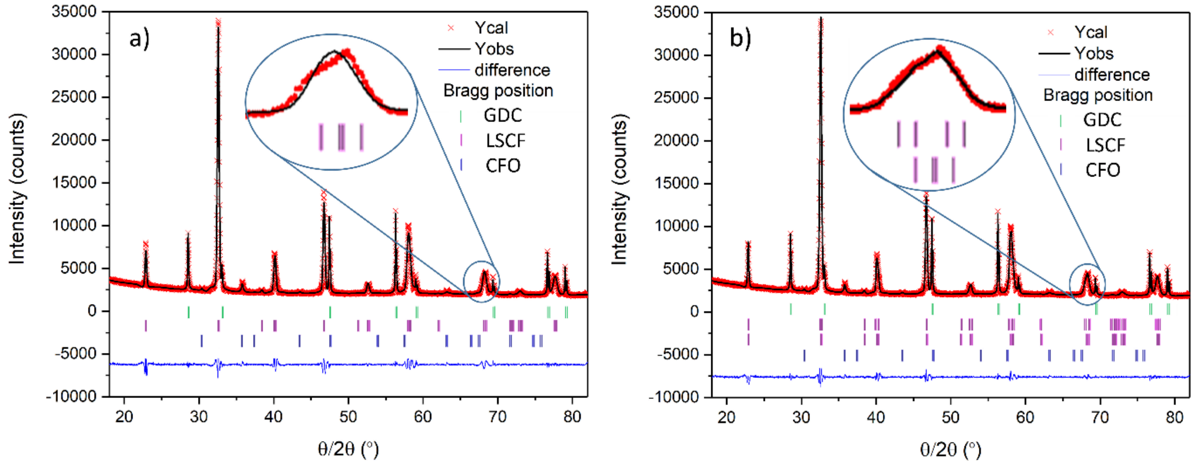

Fig. 2 XRD lattice parameter refinement of an LSCF film deposited on GDC electrolytes sintered at 900 °C for 2 h in air. a) one rhombohedral phase and b) two rhombohedral phases.

Table 1. Lattice parameters and fit parameters of LSCF fitted with one a) or two b) rhombohedral phases.

Fit	Phase	a (Å)	c (Å)	V(Å^3)	R_p	R_{wp}	R_e	Chi2
a)	$R\bar{3}c$	5.48(9)	13.50(6)	352.40(9)	16.7	13.7	5.5	6.2
b)	$R\bar{3}c$	5.48(8) 5.47(9)	13.50(2) 13.56(4)	352.25(8) 352.72(5)	12.5	9.4	5.5	2.9

In order to explore the elemental composition of the minority third phase, STEM-EDX analysis was performed on particles removed from the deposited film (Fig. 3). Elemental maps demonstrate the presence of only La, Sr, Co, Fe and O elements with the cobalt EDX map showing distinct Co-rich particles. The size of these secondary phase particles is as small as 10 nm (Fig. S. 1). EDX spectra were collected at 3 selected locations to identify the elemental composition in both the cobalt-rich and LSCF grains. The point analysis on location 1 showed predominantly Co and Fe elements with a Co:Fe ratio of ~1. Accordingly, the ICDD database of cobalt ferrite spinel structures was investigated. $CoFe_2O_4$ (ICDD: 04-006-4147) and Co_2FeO_4 (ICDD: 04-016-3952) are among the possible phases identified. As the exact composition of the spinel-type material is unknown, this will be referred to as $CoFeO_x$ (CFO) for the discussion. The point analysis in locations 2 and 3 give A-site cation ratios for La:Sr ratio of~3.7, in agreement with the ICP-OES experiments (~2.4). Similar trends were detected in the line scans of LSCF particles (Fig. S. 2). Moreover, both techniques indicate an A-site deficient perovskite with A:B site cation ratios of 0.95 ± 0.01.

Literature reports show several origins behind the B-site cation precipitation in ABO_3 type LSCF films, such as A-site deficiency[26], high-temperature annealing (1100 °C for 120 h) of LSCF contacted with YSZ[21] and chromium poisoning.[22,23] On the other hand, film preparation and deposition techniques were also shown to result in such non-stoichiometry.[11,24,25] Hayd *et al.* studied $(LaSr)CoO_{3-\delta}$ thin films deposited by the metal organic deposition (MOD) technique. Small amounts of Co_3O_4 and Ruddlesden-Popper $(LaSr)_2CoO_{4\pm\delta}$ precipitates were observed to coexist with the stable $(LaSr)CoO_{3-\delta}$ perovskite.[11] It was suggested that a phase equilibrium process might not have been reached during the deposition due to certain characteristics of the film preparation. In another work, Heel *et al.* used a flame spray synthesis method to obtain nanoscale LSC and LSCF powders.[24,25] Secondary $(LaSr)_2CoO_{4\pm\delta}$ precipitates were detected depending on the solvent mixture. The authors suggested that the solvents affected the flame properties and in turn homogeneous mixing of the elements.

As the final composition of the film was different from the targeted composition, the origins of the A-site deficiency in this work were investigated further. The discrepancy is more likely to be related to the precursor purity and/or solubility limits of the metal-nitrates as well as a non-equilibrium state where the droplets when they impact the heated substrate during the ESD coating, spread, decompose and dry more or less at the same time. It is worth mentioning that LSCF electrodes of higher La/Sr concentration (e.g. LSCF 7328 and LSCF 8228) were found to be thermodynamically more stable towards sulfur degradation than LSCF 6428.[26] Besides, the average thermal expansion coefficients (TEC) of such perovskites matches more closely to the GDC electrolyte than the benchmark LSCF 6428.[27]

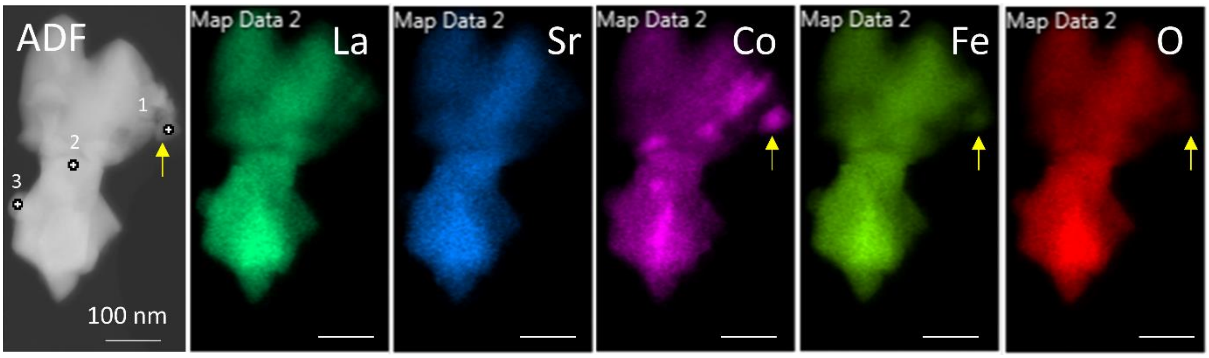

Fig. 3. STEM ADF-EDX elemental maps of the particles removed from the film. The intensity of the maps represents the net EDX counts after corrections for background and peak overlap.

To locally observe the crystal structures, growth and orientation of LSCF and CFO particles, HR-TEM was used. The micrographs were analysed as shown in Fig. 4. Fast Fourier transforms (FFT) were taken from the locations inside the square. Experimental FFTs were compared with the simulations of ICDD patterns of rhombohedral ($R3\bar{c}$) for LSCF and spinel ($Fd\bar{3}m$) for CFO. It was observed that the LSCF grain was oriented in the $[\bar{1}11]$ zone axis, whereas the spinel phase was in the [112] zone axis. The arrows indicate the lattice spacing values for LSCF ($1\bar{1}2$) and CFO ($11\bar{1}$).

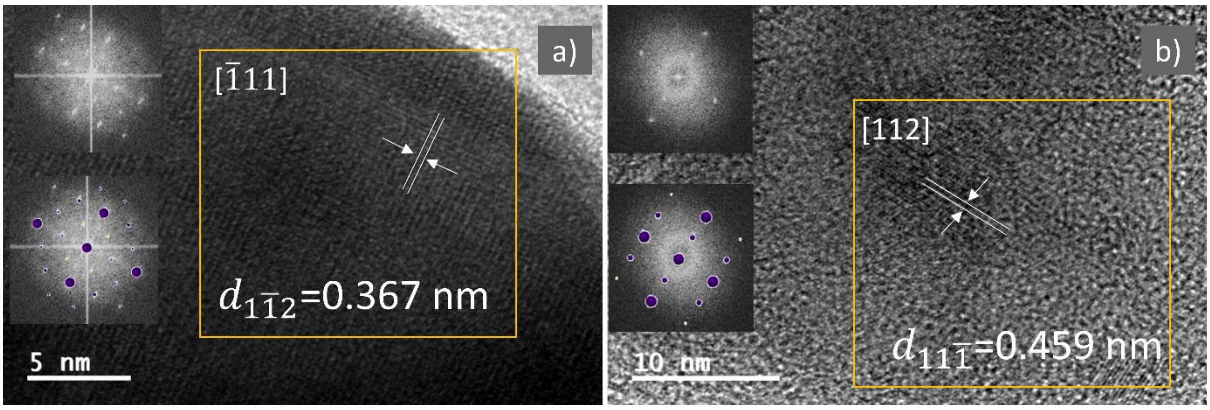

Fig. 4. HRTEM micrographs and corresponding FFTs and simulations of a) rhombohedral LSCF and b) spinel CFO phase.

Fig. 5 shows the electrochemical characteristics of LSCF films deposited symmetrically on GDC electrolyte determined by impedance spectroscopy in the temperature range of 450-650 °C in air and under OCV conditions. The Arrhenius plot showing the temperature dependence of the total polarisation losses (Fig. 5a) exhibits linear behaviour with an activation energy of 1.5 eV, which is comparable to those reported in the literature for LSCF-based cathodes of similar compositions contacted with GDC electrolytes.[28,29] Fig. S. 3 shows the Nyquist plots of impedance responses measured at OCV at 450-650 °C. The resistance values were determined by deducting the high-frequency intercept from the low frequency on the real axis in the impedance plane. Since the measurements were performed on symmetrical cells, the resistance value was divided by two and then multiplied by the surface area (~2 cm^2) of the electrode films.

The plots show remarkably low ASR values of 0.037, 0.100, and 0.320 Ω cm^2 at 650, 600 and 550 °C, respectively. Such small impedances make the equivalent circuit fitting extremely difficult especially when considerable inductive effects coexist with a very high series resistance of the electrolyte. However, at least two elementary contributions are visible. The resistance at the low-frequency region was observed as a separate arc and is independent of the measurement temperature. Following the calculations of gas diffusion layer thickness (~ 1 mm), the main contribution to the resistance associated with gas diffusion was attributed to the bulk diffusion in the gas layer at the electrode surface.[30] Therefore, the high-frequency semicircle was associated with the cathodic polarisation losses. In previous work, we studied the influence of sintering temperature on the electrochemical properties of similar LSCF-based films.[31] The impedance spectra showed that the charge-transfer resistance at the high-frequency semicircle was convoluted with the non-charge transfer processes (solid-state transport and oxygen surface exchange). However, as the chemical capacitance values of this semicircle (~10^{-2} - 10^{-3} F cm^{-2}) were one-to-two orders of magnitude higher than the typical double layer capacitance values (< 10^{-4} F cm^{-2}), the limiting reaction steps of these LSCF-based films were attributed to non-charge-transfer reactions.

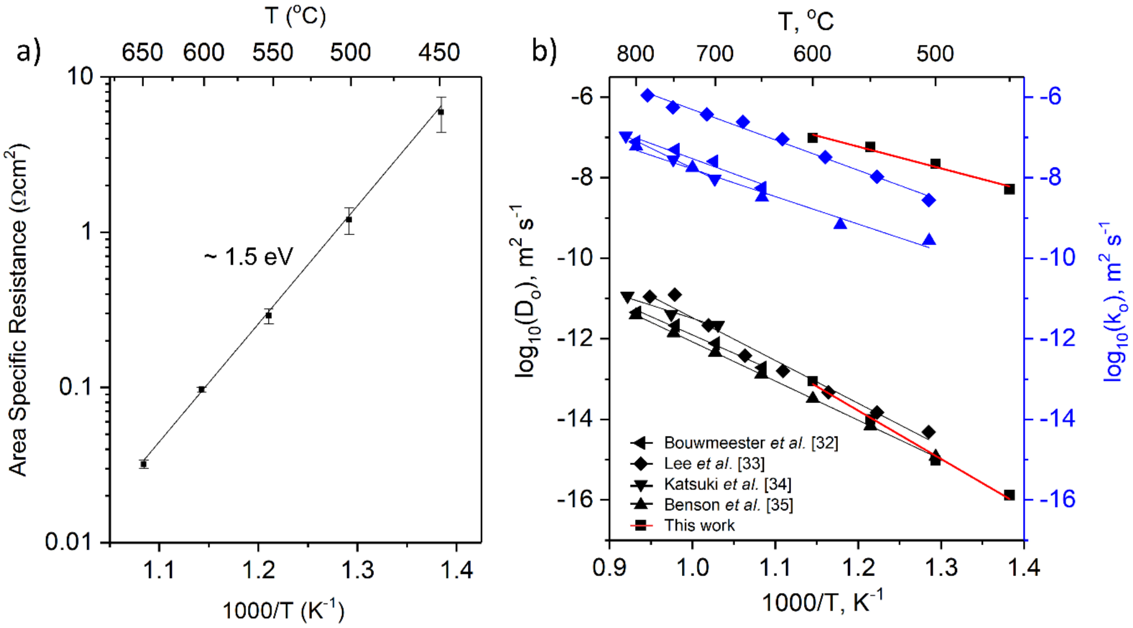

Fig. 5. a) Arrhenius plot of area specific resistance values of three LSCF films (sintered at 900 °C for 2 h) on GDC electrolytes. b) Oxygen self-diffusion (D_o) and surface exchange coefficients (k_o) calculated from the electrochemical impedance data and compared with literature data measured by different methods.[32–35]

The catalytic activity of CFO nanoparticles on ORR kinetics was examined with a complementary set of experiments. CFO solution was infiltrated into the bare stoichiometric LSCF 6428 (Sigma-Aldrich, 10-14 m^2 g^{-1}) electrode. The infiltration method was chosen to mimic the percentage and small particle sizes of CFO similar to those observed in the ESD deposited films. The stoichiometric LSCF was chosen to separate the effects of A-site non-stoichiometry and the possible catalytic activity of CFO nanoparticles. A substantial decrease in both ASR and activation energy (E_a) was observed at the initial stages of the experiment (low-temperature operation), suggesting the catalytic activity of CFO nanoparticles (Fig. S. 4). As the temperature increased, both ASR and E_a of the infiltrated film began to behave very similarly to the bare film. This can be attributed to the agglomeration of CFO particles as observed in Fig. S. 6, which is a commonly observed problem with the infiltration method. As observed in Fig. S. 5, both the resistance and E_a associated with the bulk diffusion and surface exchange related resistance were decreased with CFO infiltration. It seems that CFO nanoparticles have a synergistic effect on the overall ORR kinetics. This experiment suggested that CFO nanoparticles might have catalytic activity as long as agglomeration and coarsening effects are controlled. As such problems were not observed in our films, LSCF surfaces decorated with CFO nanoparticles appear to offer catalytic enhancement for SOFC cathode applications.

Oxygen self-diffusion (D_o) and surface exchange coefficients (k_o) were calculated from the electrochemical impedance spectra using Adler Lane Steele (ALS) model for the LSCF films deposited by the ESD as symmetrical cells (refer to Supporting Info b) for the model).[36] Fig. 5b shows the D_o and k_o values determined for these LSCF electrodes and compares them to data obtained from several other LSCF 6428 samples using conductivity relaxation[32], gravimetric relaxation[34], isotope exchange[35] and impedance spectroscopy.[33] Regardless of the measurement technique as well as the compositional variations, the values of D_o show good agreement. On the other hand, significant differences in k_o values were observed. Especially, this work exhibits approximately two orders of magnitude higher k_o values than ref. [35]. If the LSCF films deposited by the ESD had similar oxygen transport parameters to that of ref. [35], ASR at 600 °C would be expected to range between 1.2 and 3.8 Ω cm^2, which is more than an order of magnitude higher than this work.

The significant spread in k_o among all LSCF 6428 data most likely indicates differences in surface composition, structures, and experimental conditions. Measurement atmosphere[37], applied bias [38] and thermodynamic effects such as strain and surface charge[39] were also shown to have an impact on the Sr segregation at the surface. Therefore, a direct comparison of k_o from different sources may not provide consistent results.

In order to see the outermost surface composition of the LSCF deposited by the ESD, low energy ion scattering (LEIS) spectroscopy was used. Fig. 6 shows the atomic composition and the chemical depth profile at the surface and sub-surface. It is important to note that surface roughness influences the scattered ion signals.[19] As this sample is quite porous and rough, quantification has not been attempted. From the trend of the normalised peak area, it is clear that there was significantly more Sr concentration and less La at the surface compared to a few nanometres below the surface. Although the B-site cation concentrations appear uniform throughout the measurement length, a slightly higher concentration of Fe and less Co at the immediate surface was observed. The significant variation of A-site cation concentrations from the surface to bulk is consistent with similar Sr-based perovskite materials[40] and suggests that the surface and sub-surface structure are rather different than in bulk.

In terms of strontium surface segregation rate, stoichiometry may play a key role. Yu *et al*. observed changes in strontium surface segregation rate following post-annealing of the heteroepitaxial LSCF thin films with varying Sr content.[41] LSCF 7328 had lower surface segregation than LSCF 6428 and LSCF 8228, respectively.

In another work, an *in situ* creation of a spinel/perovskite interface of $Co_3O_4/La_{0.3}Sr_{0.7}CoO_{3-\delta}$ by a wet-chemical method led to a reconstruction of surface Sr enrichment region.[42] This method provided the Co_3O_4 nanoparticles to be embedded in the surface of a parent perovskite without damaging the bulk structure. In comparison to a physically mixed sample, the electronic structure of the chemical composite radically changed due to strong interface interaction. This work demonstrated the activation of the surface lattice oxygen, which was previously shown to be a significant redox partner in oxygen evolution and incorporation reactions.[43]

Another important factor that may influence the chemical stability against Sr segregation is the A-site deficiency.[44] It was reported that A-site deficient $La_{0.8}Sr_{0.2}MnO_3$ (LSM) thin films showed higher stability against thermal annealing in terms of surface structures and chemistry.

All these data suggest that both the creation of a spinel/perovskite pair and the modified stoichiometry of LSCF might have contributed to the relatively lower surface segregation rate when compared to that observed in the stoichiometric LSCF 6428. Low temperatures for deposition (300 °C), film sintering (900 °C) and cell operation (< 650 °C) equally lower the segregation rate and thus lead to higher surface exchange properties.

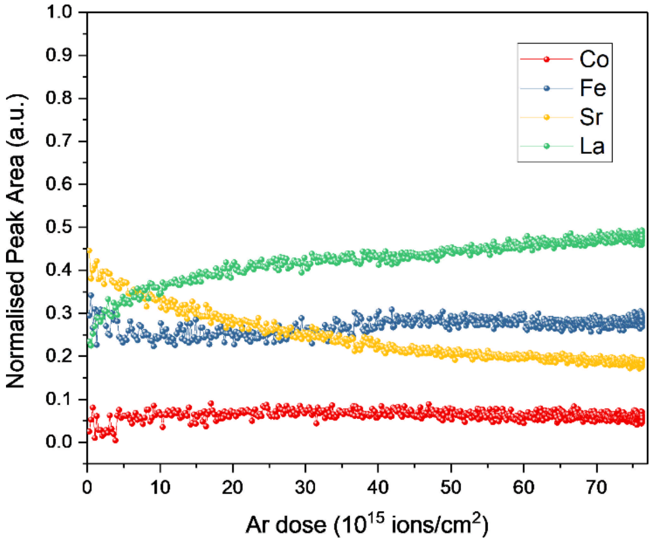

Fig. 6. 5 keV Ne^+ primary ion beam LEIS depth profiles of an LSCF film showing the normalised peak area as a function of Ar sputtering depth.

Based on the positive performance results in the symmetrical cells, the cathode films were tested on the state-of-the-art Ni-YSZ based anode-supported cell. Fig. 7a shows the current-voltage-power (I – V – P) characteristics, and the measured Nyquist plots at 0.75 V are demonstrated as a function of temperature in Fig. 7b. The power densities at 0.7 V and peak power density at each temperature are listed in Table 2. The cell yielded a peak power density of 1.4 and 1.0 W cm^{-2} and the current density at a cell voltage of 0.7 V was 1.2 and 0.7 A cm^{-2} at 650 and 600 °C, respectively. Table 3 lists the materials and peak power densities of comparably high-performance cells reported in the literature. The peak power density at 600 °C in this work is among the highest values for LSCF-based cathodes.[45,46] Unlike this work, the electrodes in references [45,46] contain an LSCF/GDC layer either as a barrier layer or as a current conducting layer. On the other hand, similar to our columnar-like LSCF cathode microstructure, Hsu *et al.* also used the ESD technique to deposit an LSCF cathode on Ni-SDC based anode-supported cells.[47] They reported a 0.9 W cm^{-2} peak power density at 600 °C with a significantly lower current density at 0.7 V in comparison to this work.

It is also worth mentioning that the estimated ASR value of a 1.5 µm-thick YSZ and 0.7 µm-thick GDC bi-layer electrolyte at 600 °C (σ_{YSZ}=0.005 S cm^{-1} and σ_{GDC}=0.020 S cm^{-1}) is 0.03 Ω cm^{-2}. Although higher than the theoretical ohmic resistance of YSZ/GDC bi-layer electrolytes, which is due to contact resistance of the setup, values indicated in Table 2 are similar to much thinner YSZ/GDC bi-layer electrolytes.[45,48] Also, the impedance diagrams were analysed by the CNLS fitting (Fig. S. 7). The ESD cathode had the lowest contribution to the total resistance under applied potential.

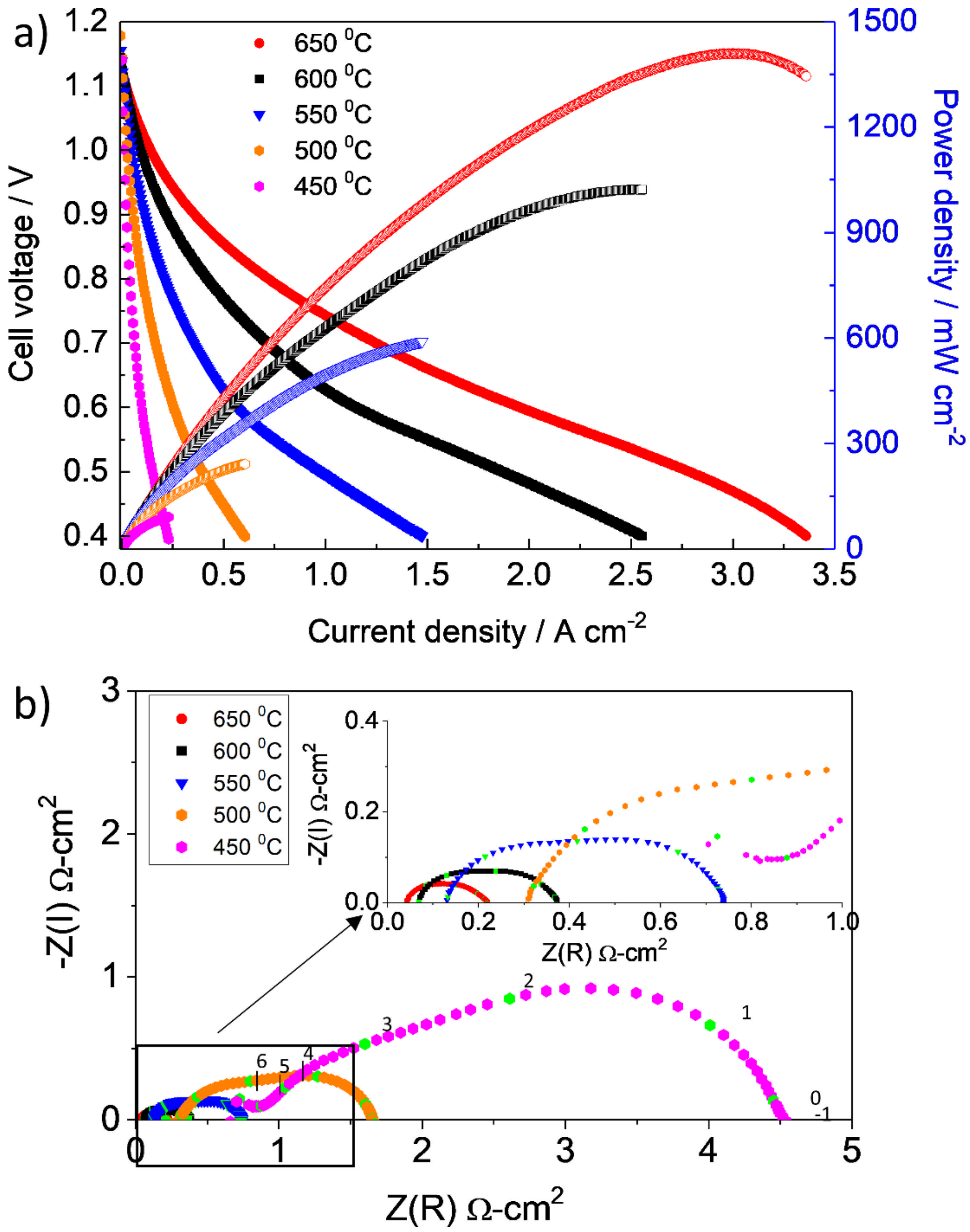

Fig. 7. I-V-P curves and corresponding Nyquist impedance plots of LSCF/GDC/YSZ/Ni-YSZ cells measured at 0.75 V with 3 % humidified hydrogen in the anode side. The green points are frequency values on a logarithmic scale.

Table 2. OCV, ohmic resistance, polarisation resistance and power density values of film sintered at 900 °C for 2 h in air between 650-450 °C with 3% H_2O in H_2 in the anode side.

T (°C)	OCV (V)	Ohm. ASR in OCV (Ω cm^{-2})	Pol. ASR in OCV (Ω cm^{2})	Power density at 0.7 V [W cm^{-2}]	Peak power density [W cm^{-2}]
650	1.12	0.04	1.34	0.87	1.40
600	1.13	0.07	2.28	0.50	1.00
550	1.14	0.13	4.22	0.25	0.59
500	1.14	0.32	8.46	0.12	0.24
450	1.14	0.70	22.14	0.05	0.09

Table 3. The performance results of this work and other high-performance anode-supported fuel cells using 3% H_2O in H_2 in the anode side.

Cathode (thickness)	Cathode deposition technique	Anode	Electrolyte	Current density at 0.7 V [A cm^{-2}]			Peak power density [W cm^{-2}] @600°C	Ref.
				550 °C	600 °C	650 °C		
LSCF[a]/GDC[b] (40 nm) and LSCF (5 µm)	SC[*] and CSD[Φ]	Ni-YSZ	YSZ[e](100 nm)/GDC(400 nm)	0.60	1.00	1.5	1.00	45
LSCF (~100 nm) and LSCF/GDC	SC and SP	Ni-YSZ	YSZ/GDC	0.44	0.80		0.97	46
LSCF (8 µm) and LSCF (8 µm)	ESD and stencil-printing	Ni-SDC[h]	SDC (15 µm)	0.22	0.40	0.66	0.91	47
A-site def. LSCF[c]	ES[¶]	Ni-BZCYYb[f]	GDC (10 µm)		0.61		0.62	49
LSCF (~100 nm) and LSCF (15 µm)	PLD and brush paint	Ni-BZCYYb4411[g]	BZCYYb4411 (15 µm)	0.42	0.67	0.98	0.52	50
LSCF	Ink-jet printing	Ni-YSZ	YSZ (10.0 µm)/GDC(0.2 µm)	0.20	0.40		0.37	51
L58SCF[d] (50 µm)	SP	Ni-YSZ	YSZ (1.0 µm)/GDC[i] (0.5 µm)	-	1.00	1.60	-	52
LSCF (6 µm) and LSCF (30 µm)	ESD and SP	Ni-YSZ	YSZ (1.5 µm)/GDC (0.7 µm)	0.35	0.71	1.20	1.00	This work

[a]LSCF: $La_{0.6}Sr_{0.4}Co_{0.2}Fe_{0.8}O_{3-\delta}$, [b]GDC: $Gd_{0.1}Ce_{0.9}O_{1.95}$, [c]A-site deficient LSCF6428: $(La_{0.6}Sr_{0.4})_{0.95}Co_{0.2}Fe_{0.8}O_{3-\delta}$, [d]L58SCF: $La_{0.58}Sr_{0.4}Co_{0.2}Fe_{0.8}O_{3-\delta}$. [e]YSZ: $Y_{0.16}Zr_{0.84}O_{1.92}$, [f]BZCYYb: $BaZr_{0.1}Ce_{0.7}Y_{0.1}Yb_{0.1}O_{3-\delta}$ (BZCYYb) [g]BZCYYb: $BaZr_{0.1}Ce_{0.7}Y_{0.1}Yb_{0.1}O_{3-\delta}$ (BZCYYb), [h]SDC: $Sm_{0.2}Ce_{0.8}O_{1.95}$. [i]GDC: $Gd_{0.2}Ce_{0.9}O_{2-\delta}$ [*]SC: Spin coating, [¶]ES: Electrospinning, [Φ]CSD: Chemical Solution Deposition

To sum up, the high performance obtained from the present LSCF film most likely results from several combined effects:

- Microstructure of the ESD films provides oxygen gas diffusion channels at multiple length scales (from a few µm to ~ 100 nm), which provides facile gas transport throughout the film, as well as high active surface area for the ORR kinetics.
- A-site deficiency leads to the precipitation B-site elements (CFO) with dimensions of a few tens of nanometres. These particles decorate the LSCF surfaces and do not show signs of agglomeration or coarsening.
- A-site non-stoichiometry also leads to alteration of the LSCF crystal structure with two-perovskites having slightly different lattice parameters evolving.
- Catalytic activity of the nano-sized B-site spinel particles is evidenced on a complementary set of experiments.
- LSCF 7328 was reported to be superior to the benchmark LSCF 6428 in terms of better matching of TEC with the electrolyte.[27] The LSCF ESD cathodes demonstrated good adherence

to the electrolyte with undetectable interfacial charge-transfer resistance, signifying good TEC matching with the electrolyte.

- Similar to other strontium-based perovskites, Sr segregation was observed by LEIS measurements in the LSCF ESD films. However, one-to-two orders of magnitude higher surface exchange coefficient (k_o) obtained in this work might be related to the relatively lower Sr segregation rate in the 5 % A-site deficient LSCF 7328 stoichiometry in comparison to stoichiometric LSCF 6428.[41]

4. Conclusions

The high electrochemical performance of ~ 100 nm sized LSCF particles was investigated focusing on the crystal structure, stoichiometry, and secondary phase precipitates. Electrostatic spray deposition (ESD) technique was used to deposit LSCF. The films were A-site deficient with an average stoichiometry of $(La_{0.7}Sr_{0.3})_{0.95}Co_{0.2}Fe_{0.8}O_{3-\delta}$. The XRD showed a closely related two-phase perovskite structure for LSCF as well as a precipitation of a minority ~$CoFeO_x$ (CFO) spinel phase with particle sizes < 50 nm after sintering at 900 °C for 2 h in air. These films gave very low ASR values of 0.037, 0.100 Ω cm^2 on symmetrical cells, and peak power densities of 1.4 W cm^{-2} and 1.0 W cm^{-2} on a Ni/YSZ anode-supported cell at 650 and 600 °C, respectively. In agreement with the literature, LEIS spectra confirmed the strontium enrichment at the outermost surface and sub-surface with respect to the bulk. However, both the creation of catalytically active spinel phase by A-site deficiency and modified stoichiometry of LSCF might account for a lower Sr surface segregation rate. Moreover, LSCF surfaces decorated with catalytically active CFO nanoparticles helps to have one-to-two-orders of magnitude higher surface exchange rates. All these findings point to the conclusion that the high-performance of the LSCF films in this work is partly due to the catalytically active spinel phase created by the A-site deficiency in perovskite LSCF and partly to the nanostructured microstructure of the film.

Acknowledgements

OC and ED acknowledge the funding from the Centre of Excellence of Multifunctional Architectured Materials "CEMAM" n° AN-10-LABX-44-01 funded by the "Investments for the Future" Program. OC, EC and SJS acknowledge funding from the EPSRC grant (EP/ M014142/1). C.-A. T. and J.-W. S. acknowledge Global Frontier R&D Program on Center for Multiscale Energy Systems (Grant No. NRF-2015M3A6A7065442) of the National Research Foundation (NRF) of Korea. The authors would like to thank Consortium des Moyens Techniques Communs (CMTC, Grenoble INP, France).

Conflicts of interest

There are no conflicts to declare.

References

1 A. M. Hussain and E. D. Wachsman, *Energy Technol.*, 2019, **7**, 20–32.
2 Z. Gao, L. V. Mogni, E. C. Miller, J. G. Railsback and S. A. Barnett, *Energy Environ. Sci.*, 2016, **9**, 1602–1644.
3 J. A. Kilner and M. Burriel, *Annu. Rev. Mater. Res.*, 2014, **44**, 365–393.
4 S. Park, S. Choi, J. Shin and G. Kim, *RSC Adv.*, 2014, **4**, 1775–1781.
5 Y. Li, W. Zhang, T. Wu, Y. Zheng, J. Chen, B. Yu, J. Zhu and M. Liu, *Adv. Energy Mater.*, 2018, **1801893**, 1–9.
6 M. A. Laguna-Bercero, H. Monzón, A. Larrea and V. M. Orera, *J. Mater. Chem. A*, 2016, **4**, 1446–1453.
7 J. Emmerlich, B. M. Linke, D. Music and J. M. Schneider, *Solid State Ionics*, 2014, **255**, 108–112.
8 A. Mineshige, J. Izutsu, M. Nakamura, K. Nigaki, J. Abe, M. Kobune, S. Fujii and T. Yazawa, *Solid State Ionics*, 2005, **176**, 1145–1149.
9 F. Morin, G. Trudel and Y. Denos, *Solid State Ionics*, 1997, **96**, 129–139.
10 K. K. Hansen and K. Vels Hansen, *Solid State Ionics*, 2007, **178**, 1379–1384.

11 J. Hayd, H. Yokokawa and E. Ivers-Tiffee, *J. Electrochem. Soc.*, 2013, **160**, F351–F359.

12 N. Ni, C. C. Wang, S. P. Jiang and S. J. Skinner, *J. Mater. Chem. A*, 2019, **7**, 9253–9262.

13 W. Zhou, R. Ran, Z. Shao, W. Jin and N. Xu, *J. Power Sources*, 2008, **182**, 24–31.

14 N. H. Menzler, D. Sebold and O. Guillon, *J. Power Sources*, 2018, **374**, 69–76.

15 L. Blum, U. Packbier, I. C. Vinke and L. G. J. De Haart, *Fuel Cells*, 2013, **13**, 646–653.

16 O. Celikbilek, D. Jauffrès, E. Siebert, L. Dessemond, M. Burriel, C. L. Martin and E. Djurado, *J. Power Sources*, 2016, **333**, 72–82.

17 Ö. Çelikbilek, L. Dessemond and E. Djurado, in *ECS Transactions*, 2017, vol. 78.

18 J. Rodríguez-Carvajal, *Comm. powder Diffr. (IUCr). Newsl.*, 2001, **26**, 12–19.

19 H. H. Brongersma, M. Draxler, M. de Ridder and P. Bauer, *Surf. Sci. Rep.*, 2007, **62**, 63–109.

20 N. H. Menzler, J. Malzbender, P. Schoderböck, R. Kauert and H. P. Buchkremer, *Fuel Cells*, 2014, **14**, 96–106.

21 G. C. Kostogloudis, G. Tsiniarakis and C. Ftikos, *Solid State Ionics*, 2000, **135**, 529–535.

22 N. Ni and S. Skinner, *Solid State Ionics*, 2016, **288**, 28–31.

23 L. Zhao, J. Drennan, C. Kong, S. Amarasinghe and S. P. Jiang, *ECS Trans.*, 2013, **57**, 599–604.

24 A. Heel, P. Holtappels and T. Graule, *J. Power Sources*, 2010, **195**, 6709–6718.

25 A. Heel, P. Holtappels, P. Hug and T. Graule, *Fuel Cells*, 2010, **10**, 419–432.

26 S. Darvish, C. C. Wang, S. P. Jiang and Y. Zhong, *Electrochim. Acta*, 2018, **287**, 68–77.

27 V. V Kharton, F. M. Figueiredo, N. L, E. N. Naumovic, A. V Kovalevsky, A. A. Yaremchenko, A. P. Viskup, A. Carneiro, F. M. Marques and J. D. Frade, *J. Mater. Sci.*, 2001, **36**, 1105–1117.

28 D. Marinha, L. Dessemond, J. S. Cronin, J. R. Wilson, S. A. Barnett and E. Djurado, *Chem. Mater.*, 2011, **23**, 5340–5348.

29 D. Beckel, U. Muecke, T. Gyger, G. Florey, A. Infortuna and L. Gauckler, *Solid State Ionics*, 2007, **178**, 407–415.

30 J. Nielsen, T. Jacobsen and M. Wandel, *Electrochim. Acta*, 2011, **56**, 7963–7974.

31 O. Celikbilek, E. Siebert, D. Jauffrès, C. L. Martin and E. Djurado, *Electrochim. Acta*, 2017, **246**, 1248–1258.

32 H. J. M. Bouwmeester, M. W. Den Otter and B. A. Boukamp, *J. Solid State Electrochem.*, 2004, **8**, 599–605.

33 S.-N. Lee, A. Atkinson and J. A. Kilner, *J. Electrochem. Soc.*, 2013, **160**, F629–F635.

34 M. Katsuki, S. S. Wang, M. Dokiya and T. Hashimoto, *Solid State Ionics*, 2003, **156**, 453–461.

35 S. J. Benson, *PhD Thesis*, 1999, Department of Materials, Imperial College London.

36 S. Adler, J. Lane and B. Steele, *J. Electrochem. Soc.*, 1996, **143**, 3554–3564.

37 M. Niania, R. Podor, T. Ben Britton, C. Li, S. J. Cooper, N. Svetkov, S. Skinner and J. Kilner, *J. Mater. Chem. A*, 2018, **6**, 14120–14135.

38 M. Finsterbusch, A. Lussier, J. A. Schaefer and Y. U. Idzerda, *Solid State Ionics*, 2012, **212**, 77–80.

39 H. Ding, A. V. Virkar, M. Liu and F. Liu, *Phys. Chem. Chem. Phys.*, 2013, **15**, 489–496.

40 Z. Feng, W. T. Hong, D. D. Fong, Y. L. Lee, Y. Yacoby, D. Morgan and Y. Shao-Horn, *Acc. Chem. Res.*, 2016, **49**, 966–973.

41 Y. Yu, K. F. Ludwig, J. C. Woicik, S. Gopalan, U. B. Pal, T. C. Kaspar and S. N. Basu, *ACS Appl. Mater. Interfaces*, 2016, **8**, 26704–26711.

42 X. Wang, Z. Pan, K. Huang, Y. Cong, R. Cao, R. Sarangi, L. Li, G. Li and S. Feng, *Angew. Chemie Int. Ed.*, , DOI:10.1002/ange.201905543.

43 D. N. Mueller, M. L. MacHala, H. Bluhm and W. C. Chueh, *Nat. Commun.*, 2015, **6**, 1–8.

44 W. Lee and B. Yildiz, *ECS Trans.*, 2013, **57**, 2115–2123.

45 E. O. Oh, C. M. Whang, Y. R. Lee, S. Y. Park, D. H. Prasad, K. J. Yoon, J. W. Son, J. H. Lee and H. W. Lee, *Adv. Mater.*, 2012, **24**, 3373–3377.

46 I. Jang, S. Kim, C. Kim, H. Yoon and T. Song, *J. Power Sources*, 2018, **392**, 123–128.

47 C.-S. S. Hsu, B.-H. H. Hwang, Y. Xie and X. Zhang, *J. Electrochem. Soc.*, 2008, **155**, B1240–B1243.

48 H. S. Noh, K. J. Yoon, B. K. Kim, H. J. Je, H. W. Lee, J. H. Lee and J. W. Son, *J. Power Sources*, 2014, **247**, 105–111.

49 Y. Chen, Y. Bu, Y. Zhang, R. Yan, D. Ding, B. Zhao, S. Yoo, D. Dang, R. Hu, C. Yang and M. Liu, *Adv. Energy Mater.*, 2017, **7**, 1–7.

50 S. Choi, C. J. Kucharczyk, Y. Liang, X. Zhang, I. Takeuchi, H. Il Ji and S. M. Haile, *Nat. Energy*, 2018, **3**, 1–9.

51 G. D. Han, K. C. Neoh, K. Bae, H. J. Choi, S. W. Park, J. W. Son and J. H. Shim, *J. Power Sources*, 2016, **306**, 503–509.

52 F. Han, R. Mücke, T. Van Gestel, A. Leonide, N. H. Menzler, H. P. Buchkremer and D. Stöver, *J. Power Sources*, 2012, **218**, 157–162.